

---

# Cloud-cloud Collision in the Galactic Center

## 50 km s<sup>-1</sup> Molecular Cloud

Masato Tsuboi<sup>1,2</sup>, Atsushi Miyazaki<sup>3</sup>, and Kenta Uehara<sup>2</sup>

<sup>1</sup>Institute of Space and Astronautical Science, Japan Aerospace Exploration Agency,  
3-1-1 Yoshinodai, Chuo-ku, Sagamihara, Kanagawa 252-5210, Japan

<sup>2</sup>Department of Astronomy, the University of Tokyo, Bunkyo, Tokyo 113-0033, Japan

<sup>3</sup>Department of Applied Informatics, Hosei University, Kajino, Koganei, Tokyo 184-8584,  
Japan

\*E-mail: tsuboi@vsop.isas.jaxa.jp

Received (12-Dec-2014); Accepted (29-Jul-2015)

### Abstract

We performed a search of star-forming sites influenced by external factors, such as SNRs, HII regions, and cloud-cloud collisions, to understand the star-forming activity in the Galactic center region using the NRO Galactic Center Survey in SiO  $v = 0, J = 2 - 1$ , H<sup>13</sup>CO<sup>+</sup>  $J = 1 - 0$ , and CS  $J = 1 - 0$  emission lines obtained by the Nobeyama 45-m telescope. We found a half-shell like feature (HSF) with a high integrated line intensity ratio of  $\int T_B(\text{SiO } v = 0, J = 2 - 1)dv / \int T_B(\text{H}^{13}\text{CO}^+ J = 1 - 0)dv \sim 6 - 8$  in the 50 km s<sup>-1</sup> molecular cloud, which is a most conspicuous molecular cloud in the region and harbors an active star-forming site seen as several compact HII regions. The high ratio in the HSF indicates that the cloud contains huge shocked molecular gas. The HSF is also seen as a half-shell feature in the position-velocity diagram. A hypothesis explaining the chemical and kinetic properties of the HSF is that the feature is originated by a cloud-cloud collision (CCC). We analyzed the CS  $J = 1 - 0$  emission line data obtained by Nobeyama Millimeter Array to reveal the relation between the HSF and the molecular cloud cores in the cloud. We made a cumulative core mass function (CMF) of the molecular cloud cores within the HSF. The CMF in the CCC region is not truncated at least up to  $\sim 2500M_\odot$  although the CMF of the non-CCC region reaches the upper limit of  $\sim 1500M_\odot$ . Most massive molecular cores with  $M_{\text{gas}} > 750M_\odot$  are located only around the

ridge of the HSF and adjoin the compact HII region. These may be a sign of massive star formation induced by CCC in the Galactic center region.

**Key words:** Galaxy: center — stars: formation—ISM: molecules — ISM: supernova remnants

---

## 1 Introduction

The Central Molecular Zone (CMZ) (Morris & Serabyn 1996) is the Galactic counterpart of the central molecular cloud condensation often observed in nearby spiral galaxies (e.g. Sakamoto et al. 2011). The molecular clouds in the CMZ are much denser, warmer, and more turbulent than those in the disk. There are young and highly luminous star clusters in the CMZ, for example Arches cluster and Quintuplet cluster (e.g. Figer et al. 1999, Figer et al. 2002). The star formation in the CMZ must be influenced by external factors, such as interactions with SNRs, HII regions, and cloud-cloud collisions because they are crowded in the region (e.g. Morris 1993, Hasegawa et al. 1994, Hasegawa et al. 2008). However, it is hard to know observationally how the cradle molecular clouds produce such massive clusters because these clusters have already lost the surrounding molecular materials.

There are two most conspicuous molecular cloud surrounding the Galactic Center itself, Sagittarius A\*(Sgr A\*). They are called the 20 and 50 km s<sup>-1</sup> molecular clouds after their LSR radial velocities (hereafter, 50MC and 20MC). The 50MC is located only 3' from Sgr A\*. The 50MC probably harbors a massive active star-forming site which is seen as several compact HII regions (e.g. Ekers et al. 1983, Goss et al. 1985, Yusef-Zadeh et al. 2010, Mills et al. 2011) although the 20MC is not associated with obvious HII regions. The star formation activity of the 50MC is on-going and can be spatially resolved by radio and IR observations. In addition, the 50MC is probably associated with a young SNR, Sgr A East (e.g. Tsuboi, Miyazaki, & Okumura 2009). Therefore the 50MC is the best laboratory for understanding star formation influenced by external factors in the CMZ. Moreover it may be the nearest analog of star formation in extragalactic nuclei.

In the third section, we search the evidence of interactions with SNRs, HII regions, and cloud-cloud collisions in the Sgr A region, which is a main part of the CMZ, using the Galactic Center Survey with the 45-m telescope at the Nobeyama Radio Observatory (NRO)<sup>1</sup>. We found a peculiar feature in the 50MC. In the fourth section, we make core mass function (CMF) in the cloud using the CS  $J = 1 - 0$  emission line data with Nobeyama Millimeter Array (NMA) and explore the relation between the peculiar feature and the molecular cloud cores in the cloud. Throughout this paper, we

<sup>1</sup> The Nobeyama Radio Observatory is a branch of the National Astronomical Observatory, National Institutes of Natural Sciences, Japan.

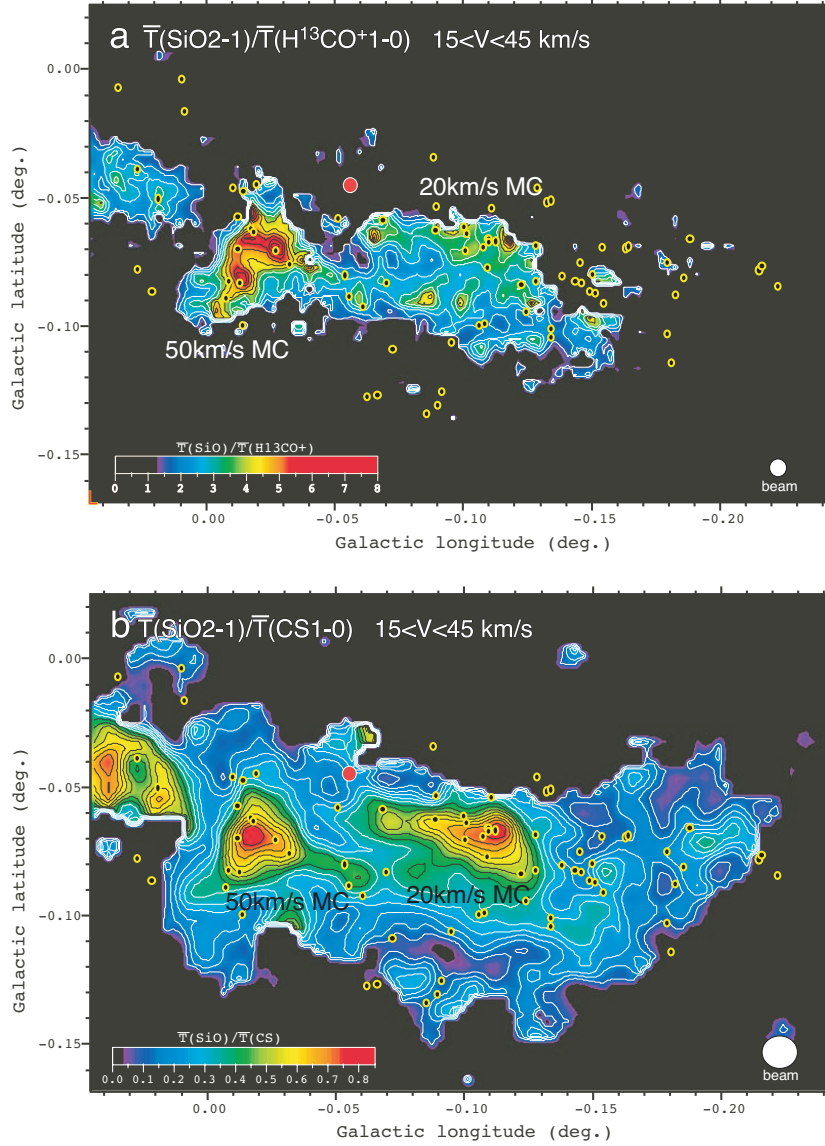


**Fig. 1. a** The 20 and 50 km s<sup>-1</sup> molecular clouds in an integrated line intensity ratio of  $\int T_B(\text{SiO } v=0, J=2-1) dv / \int T_B(\text{H}^{13}\text{CO}^+ J=1-0) dv = \bar{T}_B(\text{SiO } v=0, J=2-1) / \bar{T}_B(\text{H}^{13}\text{CO}^+ J=1-0)$ . The integrated velocity range is  $V_{LSR} = 15 - 45 \text{ km s}^{-1}$ . The angular resolution is 26". Red circle shows the position of Sgr A\*. Yellow circles show the positions of CH<sub>3</sub>OH Class I maser at 36 GHz (Yusef-Zadeh et al. 2013). **b** The 20 and 50 km s<sup>-1</sup> molecular clouds in an integrated line intensity line ratio of  $\bar{T}_B(\text{SiO } v=0, J=2-1) / \bar{T}_B(\text{CS } J=1-0)$ . The velocity range is  $V_{LSR} = 15 - 45 \text{ km s}^{-1}$ . The angular resolution is 60".

adopt 8.5 kpc as the distance to the Galactic center. Then, 24" corresponds to about 1 pc at the distance. And we use Galactic coordinates.

## 2 Observations

We used our observational datasets (channel maps) with the NRO 45-m telescope and NMA, which have been already published as other papers. A short summary of our observations is as follows; We have observed the Sgr A region in CS  $J = 1 - 0$  (48.990964 GHz) by using the NRO 45-m

telescope (Tsuboi, Handa, & Ukita 1999). We also have observed the region in SiO  $J = 2 - 1$  ( $\nu = 86.847010\text{GHz}$ ) and  $\text{H}^{13}\text{CO}^+ J = 1 - 0$  ( $\nu = 86.754330\text{GHz}$ ) emission lines by using the NRO 45-m telescope (Tsuboi et al. 2011). These are parts of the NRO Galactic Center Survey. The velocity resolution of these channel maps was  $5.0 \text{ km s}^{-1}$ . The angular resolutions were  $60''$  for the CS  $J = 1 - 0$  maps and  $26''$  for the SiO  $J = 2 - 1$  and  $\text{H}^{13}\text{CO}^+ J = 1 - 0$  maps, respectively. These correspond to about 2.5 pc and 1.1 pc at the distance to the Galactic center, respectively.

We have observed the 50MC in CS  $J = 1 - 0$  emission line by using NMA (Tsuboi, Miyazaki, & Okumura 2009). The FWHM of the element antenna of NMA is  $156''$  at 49 GHz. The velocity resolution of the channel map was  $3.8 \text{ km s}^{-1}$ . To make maps, we used the CLEAN method in the NRAO AIPS package. The size of the synthesized beam was  $8.5'' \times 10''$  ( $\phi = 24^\circ$ ) for a natural weighting, which corresponds to about  $0.35 \text{ pc} \times 0.42 \text{ pc}$  at the distance to the Galactic center. Features with spatial scales larger than  $1'$  or 2.5 pc were resolved out.

### 3 Cloud-Cloud Collision in the $50 \text{ km s}^{-1}$ Molecular Cloud

#### 3.1 Huge Shocked Molecular Gas in the $50 \text{ km s}^{-1}$ Molecular Cloud

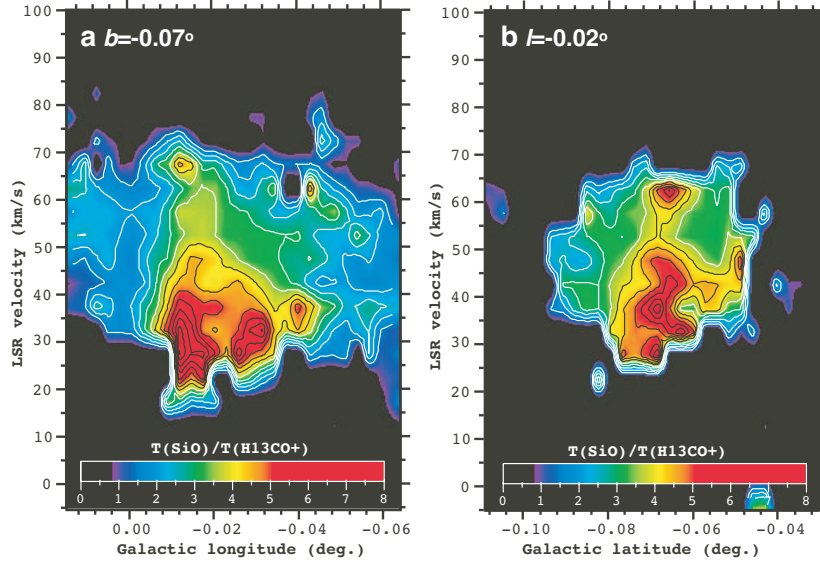
The SiO  $J = 2 - 1$  emission line is strongly detected toward the whole 50MC (see Fig.3 in Tsuboi et al. 2011). Si atom is sputtered from dust grains by non-dissociative C-shocks, which later in the gas-phase forms SiO molecule (e.g. Ziurys et al. 1989, Usero et al. 2008, Amo-Baladr3n, Mart3n-Pintado, & Mart3n 2011). The velocity width required for the ejection is  $\Delta v \gtrsim 30 \text{ km s}^{-1}$ . The SiO emission line is therefore commonly accepted to be a tracer of shocked molecular gas. The area with enhancement of SiO molecule indicates the region where shock wave propagated within  $10^5 \text{ yr}$  because the molecule is adsorbed again on dust grain during the time scale. Meanwhile the fractional abundance of  $\text{H}^{13}\text{CO}^+$  ion is not enhanced by C-shock. The SiO  $J = 2 - 1$  and  $\text{H}^{13}\text{CO}^+ J = 1 - 0$  ( $\nu = 86.754330\text{GHz}$ ) emission lines are observed simultaneously because the frequency separation between the emission lines is only 93 MHz. They are optically thin even in the Galactic center molecular cloud (e.g. Handa et al. 2006). Therefore the integrated line intensity ratio,  $R_{\text{SiO}/\text{H}^{13}\text{CO}^+} = \int T_{\text{B}}(\text{SiO } v=0, J=2-1) dv / \int T_{\text{B}}(\text{H}^{13}\text{CO}^+ J=1-0) dv = \bar{T}_{\text{B}}(\text{SiO } 2-1) / \bar{T}_{\text{B}}(\text{H}^{13}\text{CO}^+ 1-0)$ , is suitable to search for shocked molecular gas avoiding the effect of the difference of the observation conditions.

Figure 1a shows the Sgr A region in an integrated line intensity ratio of  $R_{\text{SiO}/\text{H}^{13}\text{CO}^+}$ . The integrated velocity range of the figure is  $V_{\text{LSR}} = 15 - 45 \text{ km s}^{-1}$ . The angular resolution is  $26''$ . We identify a half-shell like feature with  $R_{\text{SiO}/\text{H}^{13}\text{CO}^+} \sim 6 - 8$  in the 50MC (hereafter, HSF). The diameter of the HSF is  $D \sim 3 \text{ pc}$ . Meanwhile, there is not such feature in the 20MC. The enhancement of the ratio must be caused by the increase of the fractional abundance of SiO molecule and/or the decrease

of the fractional abundance of  $\text{H}^{13}\text{CO}^+$  molecule. The 50MC is probably associated with a massive active star-forming site as mentioned in the Introduction.  $\text{H}^{13}\text{CO}^+$  ion may be destroyed by strong UV radiation from the young massive stars. The decrease of the fractional abundance of  $\text{H}^{13}\text{CO}^+$  ion around the star-forming site produces an apparent circle feature with a high ratio of  $R_{\text{SiO}/\text{H}^{13}\text{CO}^+}$  even when the fractional abundance of SiO molecule does not increase. In this case, there is still an open question which is a dominant factor because any obvious sign of the feature is not seen both in the channel maps of SiO  $v = 0, J = 2 - 1$  and  $\text{H}^{13}\text{CO}^+ J = 1 - 0$  emission line (see Fig.4 in Tsuboi et al. 2011).

On the other hand, CS molecule is not so significantly enhanced by C-shock and is not so easy destroyed by UV radiation (see Fig.6 in Martín et al. 2012). An integrated line intensity ratio of  $R_{\text{SiO}/\text{CS}} = \int T_{\text{B}}(\text{SiO } v = 0, J = 2 - 1)dv / \int T_{\text{B}}(\text{CS } J = 1 - 0)dv$  is also an indicator of shocked molecular gas, which probably has insensibility to UV radiation. The angular resolution of the data is  $60''$ . Figure 1b shows the Sgr A region in the integrated line intensity ratio. The integrated velocity range is the same as that of figure 1a. We identify a prominent component with the high ratio of  $R_{\text{SiO}/\text{CS}}$  in the 50MC. The integrated line intensity ratio is  $R_{\text{SiO}/\text{CS}} = 0.8 \pm 0.05$  at the center position, which is three times larger than the ratio,  $R_{\text{SiO}/\text{CS}} \sim 0.3$ , in other part of the 50MC. Although the HSF clearly seen in figure 1a is almost concealed by the lower angular resolution of the CS data ( $60''$ ), it is barely identified as a curved feature in figure 1b. There is a possibility that the optical thickness of the CS emission line is somewhat large in the center region of the molecular cloud and produce a feature with a high ratio without the increase of the fractional abundance of SiO molecule. However, the half-shell morphology is hard to be produced by this effect because the optical thickness at the center position should be larger than that of the surrounding region. In addition, the integrated line intensity ratio of  $R_{\text{H}^{13}\text{CO}^+/\text{CS}} = \int T_{\text{B}}(\text{H}^{13}\text{CO}^+)dv / \int T_{\text{B}}(\text{CS})dv$  is uniformly  $\sim 0.10 - 0.15$  in the whole 50MC. There is no feature with a peculiar integrated line intensity ratio in the cloud. These rule out the possibility that the optical thickness of the CS emission line produces the feature apparently. Then these indicate that the 50MC contains huge shocked molecular gas.

There is another feature with the high ratio in the north part of the 20MC in figure 1b. The integrated line intensity ratio is  $R_{\text{SiO}/\text{CS}} = 0.8 \pm 0.05$  at the peak position, which is larger than the ratio,  $R_{\text{SiO}/\text{CS}} \simeq 0.3 \pm 0.1$ , in the south part of the 20MC. Meanwhile this feature has no significant counter part with a high ratio of  $R_{\text{SiO}/\text{H}^{13}\text{CO}^+}$  in figure 1a. Yellow circles in figures 1a and 1b show the positions of Class I methanol ( $\text{CH}_3\text{OH}$ ) maser at 36.17 GHz (Yusef-Zadeh et al. 2013). Class I methanol masers are understood to be collisionally pumped in shocks. The positions of the maser are associated with the feature. This suggests that the production of the shocked molecular gas is on-going in the feature. The feature probably contains large amount of shocked molecular gas. In



**Fig. 2.** Position-velocity diagrams of shocked molecular gas in the  $50 \text{ km s}^{-1}$  molecular cloud traced by  $T_{\text{B}}(\text{SiO})/T_{\text{B}}(\text{H}^{13}\text{CO}^+)$ . **a** Galactic longitude- velocity diagram along  $b = -0.07^\circ$ . **b** Galactic latitude- velocity diagram along  $l = -0.02^\circ$ .

addition, there is another group of the masers around  $l \sim -0.15^\circ$   $b \sim -0.08^\circ$ . This may be associated with another SiO feature with lower LSR velocity (Fig.8 in Tsuboi et al. 2012).

The difference of  $R_{\text{SiO}/\text{H}^{13}\text{CO}^+}$  between the features associating with the 20MC and 50MC may be caused by the strength of the shock. As mentioned previously, the production of the SiO molecule requires the velocity width of  $\Delta V \gtrsim 30 \text{ km s}^{-1}$  and it becomes more active with increasing of the velocity width. Typical velocity widths of the SiO and  $\text{H}^{13}\text{CO}^+$  emission lines in the 20MC are narrower than those in the 50MC (see Fig.2 in Tsuboi et al. 2011).

### 3.2 Origin of Shocked Molecular Gas in the $50 \text{ km s}^{-1}$ Molecular Cloud

Figure 2 shows the kinematic structures of the HSF traced by an integrated line intensity ratio of  $R_{\text{SiO}/\text{H}^{13}\text{CO}^+}$ . Figure 2a is the Galactic longitude- velocity diagram along  $b = -0.07^\circ$ . The HSF seen in figure 1a is also identified as a half-shell like feature with a high ratio of  $R_{\text{SiO}/\text{H}^{13}\text{CO}^+} \sim 5 - 8$  in the diagram. The velocity expanse of the feature, full width at zero-intensity (FWZI), is as large as  $\Delta V_{\text{FWZI}} \sim 50 \text{ km s}^{-1}$ . This is consistent with the velocity width required for the production of SiO molecule. Figure 2b is the Galactic latitude- velocity diagram along  $l = -0.02^\circ$ . A feature with a high ratio corresponding the HSF is also seen in the Galactic latitude- velocity diagram.

As mentioned previously, no extended HII region is detected in the 50MC although several compact HII regions are detected. At least, young massive stars in the disk region have no thermal extended SiO emission comparable to the HSF. Thermal SiO emission line are detected around a massive young star in the disk region, the Orion source I (Niederhofer, Humphreys, & Goddi 2012).



The spatial expanse of the emission line is restricted around the source I, which is less than 0.1 pc or much smaller than the distance between the compact HII regions and the HSF. The velocity expanse of the emission line is as large as  $20 \text{ km s}^{-1}$ , which is smaller than that of the HSF. In addition, although many massive young stellar objects are detected in the Sgr A region (An et al. 2011), they have no clear association with enhanced areas of thermal SiO emission line (Tsuboi et al. 2011). It is hard to explain the origin of the shocked molecular gas in the 50MC by neighboring HII region.

Figure 3a shows the positional relation between the HSF in the 50MC and the Sgr A east shell in 5-GHz radio continuum observed by VLA (contours; Yusef-Zadeh & Morris 1987). The northwestern boundary of the HSF coincides with the southeastern boundary of the Sgr A east shell. An extended component with moderate integrated line intensity ratio,  $R_{\text{SiO}/\text{H}^{13}\text{CO}^+} \sim 3 - 4$ , traces the southeastern boundary of the SNR shell. The integrated line intensity ratio probably shows that the boundary region contains shocked molecular gas. However, most of the HSF is located outside of the southeastern boundary of the SNR shell although this feature contains huge shocked molecular gas as mentioned above. The positional anti-correlation suggests that the HSF was not produced by the interaction with the SNR shell.

These kinematic features shown in Figure 2 and the appearance shown in Figure 1 indicate that the shocked molecular gas has a hollow hemisphere-like shape in the  $l - b - v$  space. The one-sided feature in the  $l - b - v$  space suggests that something impacts on one side of the molecular cloud and the induced C-shock produces huge shocked molecular gas in the cloud. The shape in the  $l - b - v$  space of the shocked molecular gas are consistent with simulations of cloud-cloud collision (CCC) (e.g. Habe & Ohta 1992, Takahira, Tasker, & Habe 2014). In the case, The velocity expanse of the feature may be as large as the velocity difference between an impactor and a cloud. If so, this is enough to produce SiO molecule by shock. The dynamical time scale is  $t = D/\Delta V_{\text{FWZI}} \sim 3\text{pc}/50\text{kms}^{-1} = 6 \times 10^4 \text{ yr}$ . This is shorter than the life time of SiO molecule in gas phase,  $10^5 \text{ yr}$ . Therefore, a probable hypothesis explaining the observed chemical and kinematic features is that the HSF is produced by CCC.

Figure 3b shows the positions of Class I methanol ( $\text{CH}_3\text{OH}$ ) maser spots at 36.17 GHz (red circles; Yusef-Zadeh et al. 2013) and 44.07 GHz (blue circles; Pihlström, Sjouwerman, & Fish 2011) observed by VLA in the the 50MC. The methanol maser spots at 36 GHz are probably located both around the HSF and the southeastern boundary to the Sgr A east shell. Meanwhile the methanol maser spots at 44 GHz are probably located on the HSF itself rather than the contact surface to the Sgr A east shell. The methanol masers at 44 GHz appear to concentrate around the northeastern boundary of the HSF. However, since the SE boundary out of the full width at half-maximum (FWHM) of the element antenna of VLA at 44 GHz, we cannot rule out a distribution of 44 GHz masers in the SE

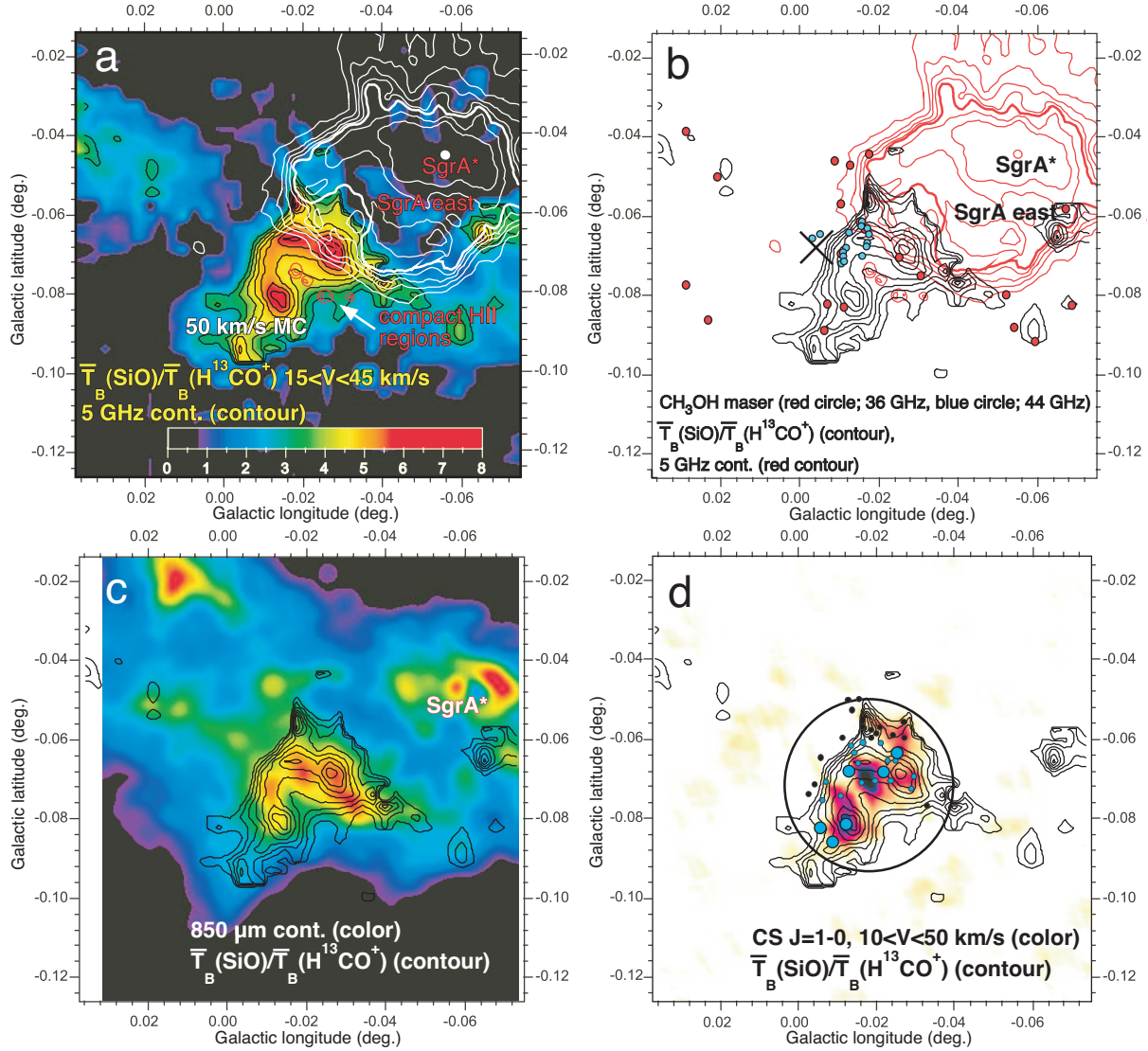


**Fig. 3.** a Relation between the 50 km s<sup>-1</sup> molecular cloud (50MC) in  $\bar{T}_B(\text{SiO}2 - 1)/\bar{T}_B(\text{H}^{13}\text{CO}^+1 - 0)$  (pseudo color) and the Sgr A east (SgrAE; white contours) in 5-GHz radio continuum with VLA (Yusef-Zadeh & Morris 1987). The compact HII regions are also shown (red contours; Yusef-Zadeh et al. 2010). The integrated velocity range of the integrated line intensity ratio is  $V_{LSR} = 15 - 45$  km s<sup>-1</sup>. b Blue circles shows the positions of 44 GHz class I CH<sub>3</sub>OH masers (Pihlström, Sjouwerman, & Fish 2011). Red circles shows the positions of 36 GHz class I CH<sub>3</sub>OH masers (Yusef-Zadeh et al. 2013) for comparison. Cross indicates the reference position where very high gas temperature  $> 300$  K, has been reported based on NH<sub>3</sub> observations (Mills & Morris 2013). c Relation between the 50MC in  $\bar{T}_B(\text{SiO}2 - 1)/\bar{T}_B(\text{H}^{13}\text{CO}^+1 - 0)$  (black contours) and in 850 μm continuum with JCMT (pseudo color; Pierce-Price et al. 2000). d Filled circles shows the positions of identified molecular cloud cores overlaid on the integrated intensity map of the CS  $J = 1 - 0$  emission line with NMA (Tsuboi, Miyazaki, & Okumura 2009). Molecular cloud cores which are probably included in the half-shell like feature are shown as blue circles. Large blue symbols show massive molecular cores with  $M_{\text{gas}} > 400 M_{\odot}$ . Other molecular cloud cores are shown as black circles. A large circle shows the full width at half-maximum (FWHM) of the element antenna of the NMA at 49 GHz.



boundary either. The Class I methanol maser at 44 GHz is also pumped collisionally by shock wave. However, the methanol maser at 44 GHz requires more extreme conditions for number density and temperature than those of the methanol maser at 36 GHz (Pihlström, Sjouwerman, & Fish 2011). They probably indicate the position of propagating shock wave at present. The concentration of the methanol maser spots at 44 GHz around the northeastern boundary of the HSF supports that the HSF was originated by CCC. In addition, cross in the figure indicates the center position of the area with very high gas temperature,  $T > 300$  K, which is detected in the observation of  $\text{NH}_3$  methastable lines (Mills & Morris 2013). This area is probably associated with the concentration of the methanol maser spots at 44 GHz.

Figure 3c shows the positional relation between the 50MC in  $R_{\text{SiO}/\text{H}^{13}\text{CO}^+}$  and in 850  $\mu\text{m}$  continuum emission with JCMT (Pierce-Price et al. 2000), which indicates the distribution of dust. The 850  $\mu\text{m}$  continuum emission traces the HSF very well. The sub-mm flux is proportional to the product of the dust temperature and column density of the dust assuming that the emission is optically thin. We also assume that the gas-to-dust ratio is not change in the cloud. If the morphology of 850  $\mu\text{m}$  continuum is mainly controlled by the column density change of the dust rather than the dust temperature change, the sub-mm morphology should resemble that of the molecular cloud itself, which are traced by CS or  $\text{H}^{13}\text{CO}^+$  emission lines, rather than that of  $R_{\text{SiO}/\text{H}^{13}\text{CO}^+}$ . On the other hand, if the morphology were to be controlled by the dust temperature change, then the sub-mm morphology would trace the site of heating of the dust. This suggests the shock heating of the dust by a CCC.

## 4 Molecular Cloud Cores in the Cloud-cloud Collision Spot

### 4.1 Identification of Molecular Cloud Cores

We used the *clumpfind* algorithm (Williams et al. 1994) to automatically identify the molecular cores in the 50MC. The channel maps, the detail procedure of core identification, and the list of identified molecular cloud core already have been shown in the previous papers (Tsuboi, Miyazaki, & Okumura 2009, Tsuboi & Miyazaki 2012b). In the case of molecular cores in the disk region, the finding method based on optically thin dust emission observation is seem to be superior to that based on emission line observation (e.g. Pineda et al. 2009). However, the Galactic center molecular clouds are too crowded to suffer from confusion when using the former method. The later method is barely available because this separates the cores with the different radial velocity to the different channel maps.

We analyzed the molecular cloud core list to explore any influence of the CCC on star formation in the 50MC. Figure 3d shows the position of the molecular cloud cores overlaid on the integrated

intensity map of the CS  $J = 1 - 0$  emission line with NMA (Tsuboi, Miyazaki, & Okumura 2009). Molecular cloud cores which are located in the HSF (black contour) are shown as blue circles. We identified 21 cores in the HSF. We supposed that these molecular cloud cores are contained physically in the spot of the CCC. Molecular cloud cores which are located outside of the HSF are shown as black circles in the figure. They mostly belong to the interacting region with the Sgr A east shell. The positions of the molecular cloud cores and the judgements of whether they are located in the spot of the CCC or not are summarized in Table 1. We use "  $R_{\text{SiO}/\text{H}^{13}\text{CO}^+} > 4$  or  $< 4$  at the center position of the core" as the criterion of the judgement because it is hard to find  $R_{\text{SiO}/\text{H}^{13}\text{CO}^+} > 4$  in the area except for the HSF (see Fig.1 and Fig.3a). The radial velocities, peak brightness temperatures with the correction of the primary beam attenuation of the NMA, half width at half-maximum (HWHM) radius and FWHM velocity widths (also see Tsuboi & Miyazaki 2012b) are also summarized in Table 1. To estimate the HWHM radius, we subtracted the physical resolution from the observed radius,  $R_o$ :  $R = (R_o^2 - r_{\text{beam}}^2)^{1/2}$ , where  $r_{\text{beam}}$  is the physical resolution;  $r_{\text{beam}} = \frac{\sqrt{0.35 \times 0.45}}{2} = 0.2$  pc.

#### 4.2 Mass Estimation of Molecular Cloud Cores

The molecular gas mass of the identified cores is re-estimated from the CS  $J = 1 - 0$  emission line intensity under the LTE condition. The molecular column density traced by the CS  $J = 1 - 0$  emission line with the optical thickness of  $\tau$  is given by

$$N_{\text{mol}}(\tau)[\text{cm}^{-2}] = \frac{7.55 \times 10^{11} T_{\text{ex}} \int T_{\text{B}} dv [\text{K kms}^{-1}]}{X(\text{CS})} \times \frac{\tau}{1 - e^{-\tau}}. \quad (1)$$

Here,  $\tau$  is the optical thickness of the CS  $J = 1 - 0$  emission line;  $X(\text{CS})$  is the fractional abundance,  $X(\text{CS}) = N(\text{CS})/N_{\text{mol}}$ , which is the relative abundance of CS molecules to total molecules;  $T_{\text{ex}}$  is the excitation temperature of the CS  $J = 1 - 0$  emission line. These parameters are likely to be different from core to core. The  $\tau$  in the 50MC had been estimated to be  $\tau \sim 1 - 3$  using the comparison between the emission line intensities of the major and minor isotopes (Liu et al. 2013). Here, we assumed that the molecular cores have a single optical thickness of  $\tau = 1.7$ . If so, the remaining error by the optical thickness should be suppress to be less than  $\pm 50\%$ . Using RADEX LVG program (van der Tak et al. 2007) based on CS  $J = 1 - 0$  and  $2 - 1$  emission line data in the 50MC (CS  $J = 1 - 0$ ; Tsuboi, Handa, & Ukita 1999, CS  $J = 2 - 1$ ; Tsuboi, Ukita, & Handa 1997, Bally et al. 1987), the  $T_{\text{ex}}$  and  $X(\text{CS})$  of the cores are evaluated. We assumed that the molecular cores have the single gas kinetic temperature of  $T_{\text{K}} = 80$  K (e.g Mills & Morris 2013). Figure 4 shows the calculated relations between the brightness temperature ratio of the CS  $J = 1 - 0$  and CS  $J = 2 - 1$  emission lines,  $T_{\text{B}}(\text{CS } J = 2 - 1)/T_{\text{B}}(\text{CS } J = 1 - 0)$  and the brightness temperature of the CS  $J = 1 - 0$  emission line on the plane of  $\text{H}_2$  number density,  $n_{\text{H}_2}$ , versus CS fractional abundance per velocity

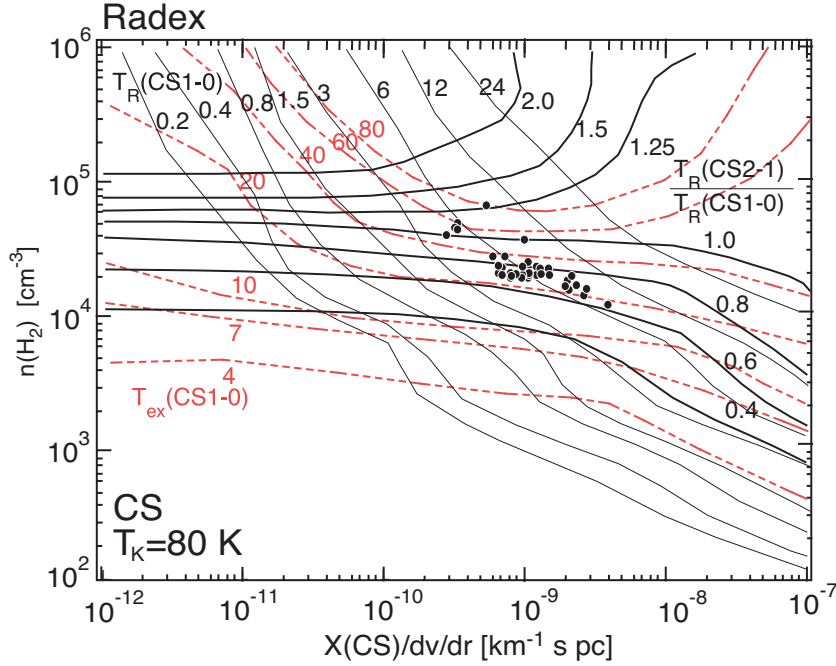


**Fig. 4.** The curves of the CS  $J = 1 - 0$  brightness temperatures,  $T_B(\text{CS } J = 1 - 0)$  (black thin lines) and the brightness temperature ratio,  $T_B(\text{CS } J = 2 - 1)/T_B(\text{CS } J = 1 - 0)$  (black thick lines) are shown on the plane of  $\text{H}_2$  number density vs. CS fractional abundance per velocity gradient. The curves are calculated by the RADEX program at a kinetic temperature of  $T_K = 80$  K. Filled circles show the identified CS molecular cores in the 50MC. The curves of the excitation temperature (red broken lines),  $T_{\text{ex}}(\text{CS } J = 1 - 0)$  are also shown.

gradient,  $X(\text{CS})/(dv/dr)$ . The figure also shows the curves of the excitation temperature of CS  $J = 1 - 0$  emission line on the plane of  $n_{\text{H}_2}$  versus  $X(\text{CS})/(dv/dr)$ . Filled circles in the figure show the identified CS molecular cores in the 50MC. They have large scatters of  $T_{\text{ex}} = 20 - 80$  K and  $X(\text{CS}) = 0.5 - 9 \times 10^{-8}$ , respectively. These corrections are applied to the LTE masses. They are also summarized in Table 1.

We calculate LTE molecular gas mass of the core from the derived distribution of the molecular column density. The molecular gas mass is given by

$$M_{\text{gas}}[M_{\odot}] = \Omega[\text{cm}^2] \mu[M_{\odot}] \sum_m \sum_n N_{\text{mol}}(m, n, \tau)[\text{cm}^{-2}], \quad (2)$$

where  $\Omega$  is the physical area corresponding to the data grid,  $\Omega = 6.44 \times 10^{34} \text{cm}^2$  for a  $2''$  grid spacing of the data cube and  $\mu$  is the mass of one particle with mean molecular weight of 2.3; thus,  $\mu = 1.94 \times 10^{-57} M_{\odot}$ . The range and mean of the molecular gas mass are  $M_{\text{gas}} = 1.8 \times 10^2 - 6.1 \times 10^3 M_{\odot}$  and  $\overline{M}_{\text{gas}} = 1.1 \times 10^3 M_{\odot}$ , respectively. The molecular gas masses are summarized in Table 1.

We also estimate the molecular gas mass by using the virial theorem assuming no external pressure and no magnetic field. The virial theorem mass of a spherical cloud with uniform density is nominally given by

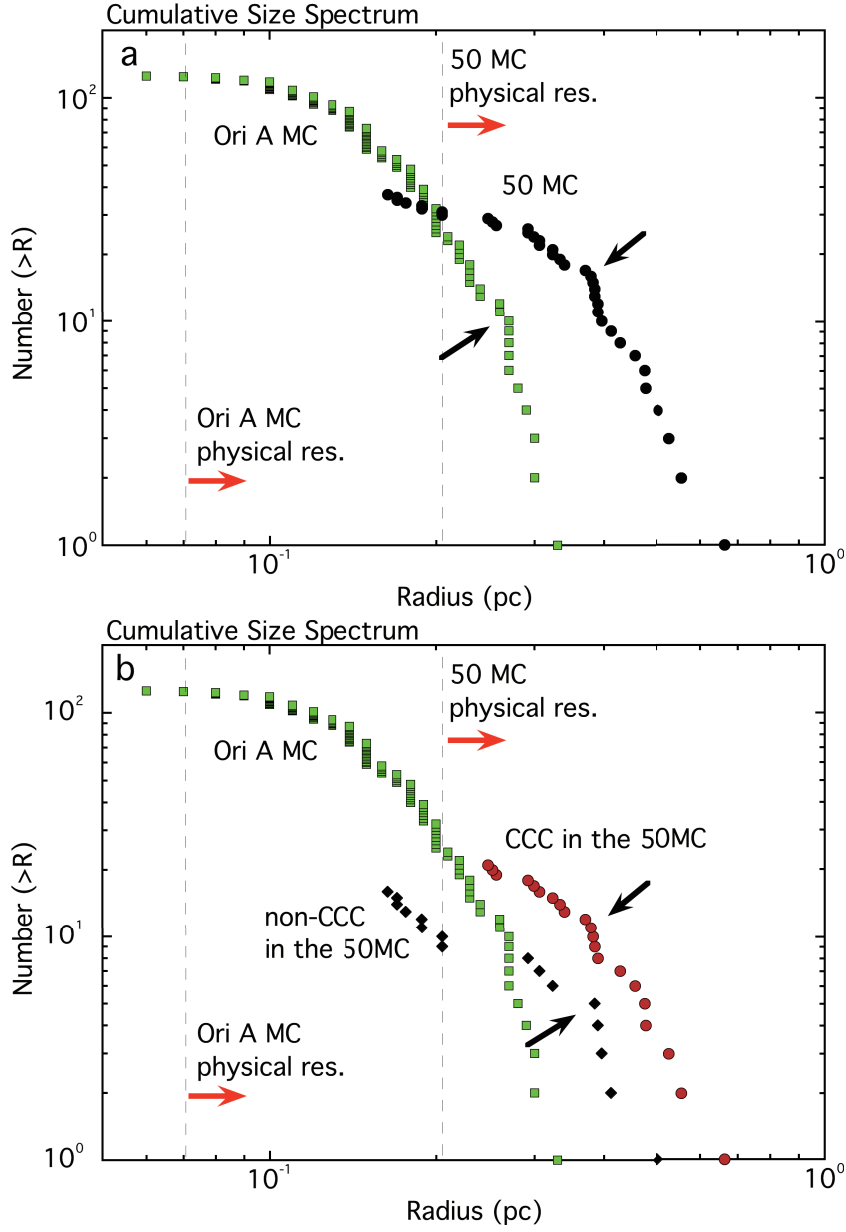
$$M_{\text{vir}}[M_{\odot}] = 210 \times \Delta V_{1/2}[\text{kms}^{-1}]^2 R[\text{pc}] \quad (3)$$

where  $\Delta V_{1/2}$  is the FWHM of a Gaussian emission line profile with the correction of the optical thickness. The range and mean of the observed velocity width of the cores are  $\Delta V_{1/2} = 2.9 - 12.9$  km s<sup>-1</sup> and  $\overline{\Delta V}_{1/2} = 7.8 \pm 2.5$  km s<sup>-1</sup>, respectively. The range and mean of the virial theorem mass in the CS  $J = 1 - 0$  emission line are  $M_{\text{vir}} = 2.4 \times 10^2 - 1.5 \times 10^4 M_{\odot}$  and  $\overline{M}_{\text{vir}} = 5.2 \times 10^3 M_{\odot}$ , respectively. The ratio,  $\alpha = M_{\text{vir}}/M_{\text{gas}}$ , indicates the relation between the virial theorem mass and the LTE molecular gas mass. The mean of the ratio is  $\bar{\alpha} = 6.9 \pm 1.7$ . They are also summarized in Table 1. This indicates nominally that the cores are not bounded without any external pressure. Although similar situation has been reported for larger-scale molecular clumps in the CMZ (e.g. Miyazaki & Tsuboi 2000), what is the external pressure for bounding of the cores in the cloud is still an open question.

#### 4.3 Size Spectrum of Molecular Cloud Cores

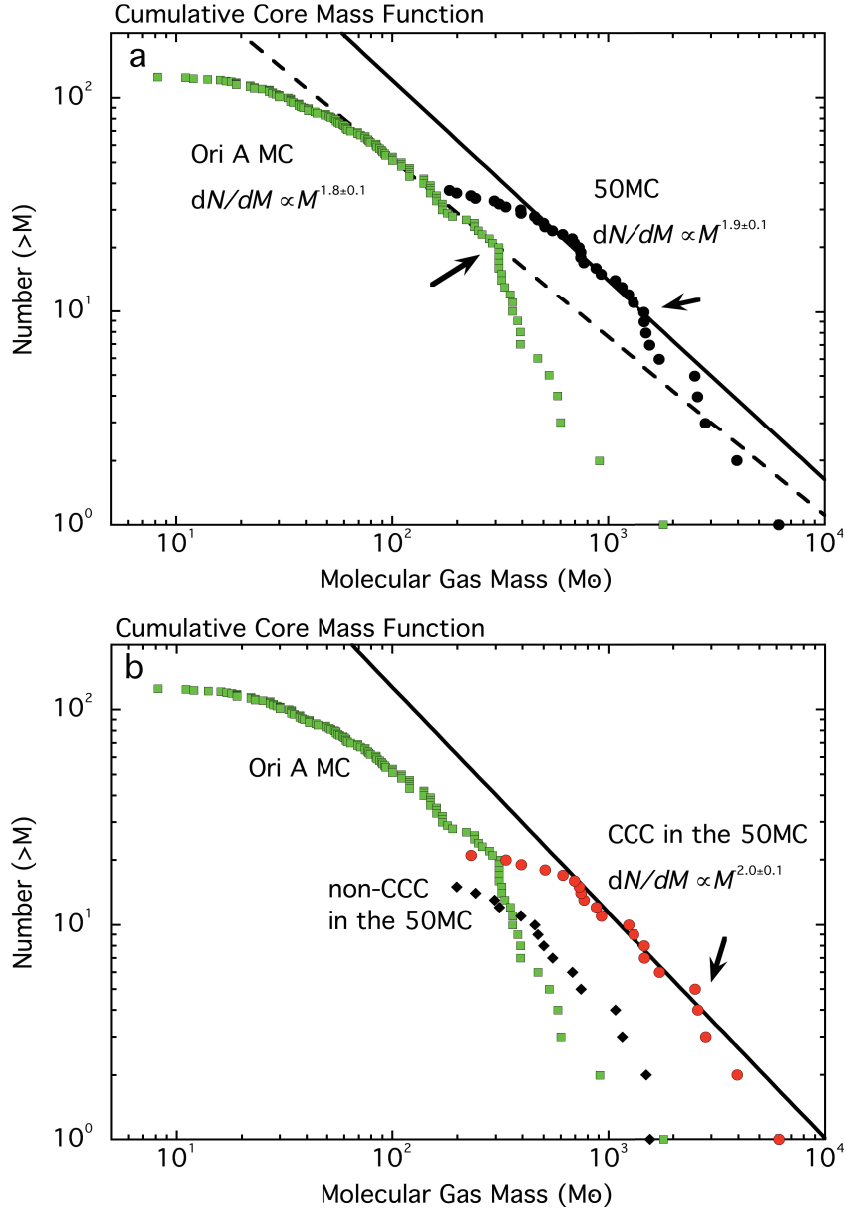
Figure 5a shows the cumulative size spectrum (SS) of the molecular cloud cores within the 50 km s<sup>-1</sup> molecular cloud (50MC). The cumulative SS of the Ori A molecular cloud is also shown in the figure for comparison (Tatematsu et al. 1993). The 50MC is a factor 20 more distant than the OriAMC, while the effective angular beam size of our data is 6 times sharper than that of the OriAMC data because of the sparse sampling of the OriAMC data. There is still a factor 3 difference between the physical effective resolutions. The physical resolutions are indicated as vertical broken lines in the figure. The cumulative SSs of the 50MC and OriAMC have breaks at  $R \sim 0.37$  pc and  $R \sim 0.25$  pc, respectively. The truncations generally means that a radius of the molecular cloud cores reaches any upper limit. The mean radius of the detected cores in the 50MC,  $\bar{R} = 0.34 \pm 0.12$  pc, is twice larger than that of the OriAMC data,  $\bar{R} = 0.16 \pm 0.06$  pc (Tatematsu et al. 1993). Because the values are larger than the physical resolutions, they are not significantly affected by the limitations of the resolution. Therefore the radius of the cores in the 50MC is larger than that in the OriAMC.

Figure 5b shows cumulative SSs of the cloud-cloud collision (CCC) and non-CCC regions in the 50MC. Both SSs have similar break at  $R \sim 0.37$  pc. The mean radiuses of the detected cores in the CCC and non-CCC regions are  $\bar{R} = 0.39 \pm 0.11$  pc and  $\bar{R} = 0.28 \pm 0.11$  pc, respectively. The radius of the cores in the CCC region is slightly larger than that in the non-CCC region. However, there is a possibility that the difference of the radius is produced as artifact by the limitation of the resolution because the half number of cores in the non-CCC region are around the effective resolution.



**Fig. 5. a** Cumulative size spectrum (SS) of the molecular cloud cores within the 50 km s<sup>-1</sup> molecular cloud (50MC) is shown (black circles). The horizontal axis is the HWHM radius of each clump,  $R$ . To estimate the HWHM radius, we subtracted the physical resolution from the observed radius,  $R_o$ :  $R = (R_o^2 - r_{\text{beam}}^2)^{1/2}$ , where  $r_{\text{beam}}$  is the physical resolution;  $r_{\text{beam}} = 0.2$  pc. The physical resolution is indicated as a vertical broken line. The cumulative SS of the Ori A molecular cloud is also shown for comparison (green squares; Tatematsu et al. 1993). The cumulative SSs of the 50MC and OriAMC have breaks at  $R \sim 0.37$  pc and  $R \sim 0.25$  pc, respectively (black arrows). **b** Cumulative SSs of the cloud-cloud collision (CCC) (red circles) and non-CCC (black diamonds) regions in the 50MC are shown. Both SSs have similar breaks at  $R \sim 0.37$  pc (black arrows).





**Fig. 6. a** Cumulative core mass function (CMF) of the molecular cloud cores within the  $50 \text{ km s}^{-1}$  molecular cloud (50MC) is shown (black circles). The cumulative CMF of the Ori A molecular cloud is also shown for comparison (green squares; Tatematsu et al. 1993). The cumulative CMFs of the 50MC and OriAMC have breaks at  $M \sim 1200 M_{\odot}$  and  $M \sim 300 M_{\odot}$ , respectively (black arrows). The inclined solid line shows the best-fit power law,  $N \propto M^{-0.9 \pm 0.1} (M > 5 \times 10^2 M_{\odot})$ . The slope corresponds to a CMF of  $dN/dM \propto M^{-1.9 \pm 0.1}$ . The inclined broken line shows the best-fit power law,  $N \propto M^{-0.8 \pm 0.1} (70 M_{\odot} < M < 300 M_{\odot})$ . The slope corresponds to a CMF of  $dN/dM \propto M^{-1.8 \pm 0.1}$ .

**b** Cumulative CMFs of the cloud-cloud collision (CCC) (red circles) and non-CCC (black diamonds) regions in the 50MC are shown. There is a faint break at  $M \sim 2500 M_{\odot}$  in the cumulative CMFs of the CCC (black arrow). The inclined solid line shows the best-fit power law,  $N \propto M^{-1.0 \pm 0.1} (M > 1.2 \times 10^3 M_{\odot})$ . The slope corresponds to a CMF of  $dN/dM \propto M^{-2.0 \pm 0.1}$ .

#### 4.4 Core Mass Function of Molecular Cloud Cores

Figure 6a shows the cumulative core mass function (CMF) of the molecular cloud cores in the 50MC and also shows the cumulative CMF based on the CS  $J = 1 - 0$  emission line data of the Ori A molecular cloud (OriAMC) for comparison (Tatematsu et al. 1993). The total mass of the 50MC is  $4 - 10 \times 10^5 M_{\odot}$  derived from sub-millimeter continuum data assuming dust temperature;  $T_d = 20\text{K}$  and metallicity;  $Z_{\odot}/Z = 1$  (Pierce-Price et al. 2000). And those of CCC and non-CCC are estimated to be  $3 - 6 \times 10^5 M_{\odot}$  and  $1 - 3 \times 10^5 M_{\odot}$ , respectively (see Fig. 3c). Meanwhile the total mass of OriAMC is  $0.5 - 1 \times 10^5 M_{\odot}$  (e.g. Tatematsu et al. 1993, Nagahama et al. 1998, Johnstone & Bally 1999). Three regions have comparable total masses.

The cumulative CMF of the 50MC has a break at  $M \sim 1200M_{\odot}$  although there is other undulation (arrows in Figure 6a). We use an inflection point of the curve as the definition of “break”. The truncation in a cumulative CMF generally means that a mass of the molecular cloud cores reaches any upper limit in the mass range (e.g. Muñoz et al. 2007). Because the radius of the cores corresponding the break is larger than the beam size (see Table 1), the break is not significantly affected by the insufficient angular resolution. Meanwhile the cumulative CMF of the OriAMC has a break at  $M \sim 300M_{\odot}$ . The inclined solid line shows the best-fit power law for the cumulative CMF of the 50MC, which is  $N \propto M^{-0.9 \pm 0.1} (M > 500M_{\odot})$ . The slope corresponds to a CMF of  $dN/dM \propto M^{-1.9 \pm 0.1} (M > 500M_{\odot})$ . The derived power law slope of the CMF is flatter than that of the 50MC,  $dN/dM \propto M^{-2.6 \pm 0.1}$ , which is previously derived with the assumption of single  $T_{\text{ex}}$  (Tsuboi & Miyazaki 2012b). Meanwhile the slope of the best-fit power law of the OriAMC corresponds to a CMF of  $dN/dM \propto M^{-1.8 \pm 0.1} (70M_{\odot} < M < 300M_{\odot})$ . The power law index of the 50MC is similar to that of the OriAMC. We applied Kolmogorov-Smirnov test to the cumulative CMFs to check whether they differ. The null hypothesis that the cumulative CMF of the 50MC is the same as that of the OriAMC is rejected because of  $p < 0.001$ . The CMF in the 50MC is top-heavy as compared with that in the OriAMC.

We also made cumulative CMFs of the molecular cloud cores within the CCC and non-CCC regions in the 50MC. Figure 6b shows the cumulative CMFs and the cumulative CMF of the OriAMC for comparison. The CMF of the CCC region is not be truncated at least up to  $\sim 2500M_{\odot}$ . On the other hand, the cumulative CMF of the non-CCC region reaches the upper limit of  $\sim 1500M_{\odot}$ . The apparent break of the 50MC mentioned above is probably caused by the upper limit of the non-CCC region. The slope of the best-fit power law of the CCC region corresponds to a CMF of  $dN/dM \propto M^{-2.0 \pm 0.1} (M > 1200M_{\odot})$ . The power law index of the CCC region is similar to that of the OriAMC. The number of the cores including in the non-CCC region is too small to evaluate the slope of the

best-fit power law accurately although the slope of the non-CCC region may be also parallel that of the Ori AMC. We applied Kolmogorov-Smirnov test to the CMFs to check whether the CMFs of the CCC and non-CCC regions differ. The null hypothesis that the CMF of the CCC region is the same as that of the non-CCC region is rejected because of  $p \lesssim 0.03$ . There is a possibility that the CCC makes top-heavy CMF.

#### 4.5 Massive Molecular Cloud Cores in the Cloud-cloud Collision Spot

As mentioned above, the HSF is lying between the concentration of the methanol maser at 44 GHz and the compact HII regions (see figures 3a and 3b). The age of the compact HII regions is reported to be as young as  $10^4 - 10^5$  yr (Yusef-Zadeh et al. 2010). Five most massive molecular cores with  $M_{\text{gas}} > 750M_{\odot}$  are located only around the ridge of the HSF (see figure 3d). Less massive molecular cores are not located around the inner boundary. The positional shift of the methanol masers, the shocked molecular gas, the massive molecular cores, and the compact HII regions suggest that CCC makes the numerous massive molecular cores and transforms from usually observed truncated CMF to a top-heavy CMF (Cf. Inoue & Fukui 2013, Namekata & Habe 2011). The massive molecular cores produce consecutively many massive stars by accretion within  $10^5$  yr (e.g. Krumholz et al. 2008). There is a possibility that the 50 MC make a new luminous cluster as a cradle molecular cloud with CCC. In addition, such CCC-induced star formation has been reported to produce luminous clusters in the disk region (e.g. RCW49 and Westerlund 2: Furukawa et al. 2009, M20: Torii et al. 2011, NGC3603: Fukui et al. 2014). On the other hand, there is no massive molecular cores with  $M_{\text{gas}} > 750M_{\odot}$  in the non-CCC region (see also Table 1). The region mostly corresponds to the the interacting region with the Sgr A east as mentioned previously. The interaction seems not yet to affect the core mass in the region because the age of the SNR is as young as  $1 \times 10^4$  yr (e.g. Zhao, Morris, & Goss 2013).

Our observation using the Atacama Large Millimeter-submillimeter Array (ALMA) already started to find molecular cloud cores in the cloud and image their fine structures. This information will be crucial in resolving these issues.

## 5 Summary

We performed an analysis of star-forming sites influenced by external factors, such as SNRs and/or cloud-cloud collisions, to understand the star-forming activity in the Galactic center region using the NRO Galactic Center Survey in SiO  $v = 0, J = 2 - 1$ ,  $\text{H}^{13}\text{CO}^+ J = 1 - 0$ , and CS  $J = 1 - 0$  emission lines obtained by the Nobeyama 45-m telescope. We found a half-shell like feature with a high ratio

of  $R_{\text{SiO}/\text{H}^{13}\text{CO}^+}$  in the 50MC, which harbors an active star-forming site. The high ratio of  $\sim 6 - 8$  in the feature indicates that there is huge shocked molecular gas in the cloud. This feature is also seen as a half-shell feature in the position-velocity diagrams. A hypothesis explaining the chemical and kinetic properties is that the feature is the spot of CCC. We analyzed the CS  $J = 1 - 0$  emission line data of the molecular cloud obtained by Nobeyama Millimeter Array to explore any influence on the star formation by CCC. The cumulative CMF in the CCC region is not truncated up to  $\sim 2500M_{\odot}$ . Most massive molecular cores with  $M_{\text{gas}} \gtrsim 750M_{\odot}$  are located only around the ridge of the HSF. In addition, we identified positional shift of the spot of CCC, the massive molecular cores, and the compact HII regions. If this line means a time sequence of active star formation with CCC, the 50 MC is a cradle molecular cloud forming a new luminous cluster.

## 6 Acknowledgments

We thank Prof. Y. Kitamura at the Institute of Space and Astronautical Science and Prof. A. Habe at Hokkaido University for useful discussions. We also thank Prof. T. Handa at Kagoshima University for useful discussions in the initial phase of this study.

**Table 1. Molecular Cloud Cores in the Galactic Center 50 km s<sup>-1</sup> Molecular Cloud**

No.	$l$	$b$	$V_{\text{LSR}}$	$\Delta V$	$R$	$M_{\text{vir}}$	$T_{\text{B}}$	$X(\text{CS})$	$T_{\text{ex}}$	$M_{\text{gas}}$	$\alpha$	CCC
	[deg.]	[deg.]	[km s <sup>-1</sup> ]	[km s <sup>-1</sup> ]	[pc]	[ $M_{\odot}$ ]	[K]		[K]	[ $M_{\odot}$ ]		[y/n]
1	-0.0157	-0.0700	45.0	11	0.53	1.4e+04	9.0	6.1e-08	28	9.2e+02	15	yes
2	-0.0117	-0.0807	29.7	9.8	0.66	1.3e+04	10	2.6e-08	55	6.1e+03	2.2	yes
3	-0.0104	-0.0733	45.0	11	0.55	1.5e+04	8.4	4.5e-08	32	1.5e+03	10	yes
4	-0.0192	-0.0696	45.0	12	0.47	1.5e+04	7.0	8.8e-08	20	3.9e+02	37	yes
5	-0.0290	-0.0685	37.3	7.8	0.39	4.9e+03	7.7	6.2e-08	25	3.3e+02	15	yes
6	-0.0149	-0.0650	37.3	14	0.38	1.5e+04	6.6	8.2e-08	21	2.3e+02	67	yes
7	-0.0181	-0.0565	60.3	7.1	0.17	1.8e+03	7.8	4.4e-08	26	2.0e+02	9.2	no
8	-0.0159	-0.0558	60.3	7.6	0.31	3.7e+03	7.7	4.5e-08	33	3.9e+02	9.5	no
9	-0.0232	-0.0695	41.2	7.1	0.48	5.1e+03	5.5	1.9e-08	28	1.5e+03	3.5	yes
10	-0.0195	-0.05741	64.1	5.6	0.16	1.1e+03	7.0	2.2e-08	28	3.1e+02	3.4	no
11	-0.0244	-0.0643	48.8	8.0	0.37	5.0e+03	5.8	2.1e-08	28	7.7e+02	6.5	yes
12	-0.0267	-0.0586	41.2	8.9	0.40	6.5e+03	7.3	3.1e-08	33	7.4e+02	8.8	no
13	-0.0130	-0.0606	64.1	6.2	0.29	2.4e+03	6.1	2.2e-08	30	6.1e+02	3.9	yes
14	-0.0067	-0.0697	45.0	9.0	0.38	6.6e+03	5.9	1.8e-08	39	1.2e+03	5.3	yes
15	-0.0265	-0.0545	48.8	5.7	0.41	2.8e+03	8.4	3.1e-08	23	4.7e+02	6.0	no
16	-0.0237	-0.0580	41.2	10	0.29	6.3e+03	6.7	3.8e-08	31	5.5e+02	11	no
17	-0.0161	-0.0598	56.5	4.2	0.26	9.6e+02	6.0	1.1e-08	28	7.4e+02	1.3	yes
18	-0.0205	-0.0600	60.3	7.6	0.34	4.1e+03	5.9	2.0e-08	28	6.9e+02	5.9	yes
19	-0.0224	-0.0644	52.6	7.2	0.30	3.2e+03	5.3	1.8e-08	27	5.1e+02	6.4	yes
20	-0.0204	-0.0560	41.2	9.3	0.39	7.0e+03	7.0	2.7e-08	35	1.2e+03	6.1	no
21	-0.0125	-0.0668	60.3	7.3	0.45	5.0e+03	5.1	1.4e-08	33	1.7e+03	2.9	yes



**Table 1.** (Continued)

No.	$l$	$b$	$V_{\text{LSR}}$	$\Delta V$	$R$	$M_{\text{vir}}$	$T_{\text{B}}$	$X(\text{CS})$	$T_{\text{ex}}$	$M_{\text{gas}}$	$\alpha$	CCC
	[deg.]	[deg.]	[km s $^{-1}$ ]	[km s $^{-1}$ ]	[pc]	[ $M_{\odot}$ ]	[K]		[K]	[ $M_{\odot}$ ]		[y/n]
22	-0.0248	-0.0626	37.3	12	0.31	9.0e+03	5.4	1.0e-08	60	2.8e+03	3.2	yes
23	-0.0138	-0.0624	56.5	5.4	0.33	2.0e+03	5.2	9.3e-09	27	1.3e+03	1.5	yes
24	-0.0123	-0.0490	52.6	7.6	0.17	2.1e+03	5.6	1.3e-08	32	4.6e+02	4.5	no
25	-0.0182	-0.0585	64.1	4.9	0.19	9.5e+02	9.8	2.9e-08	30	3.0e+02	3.2	no
26	-0.0109	-0.0586	60.3	5.5	0.50	3.2e+03	5.9	1.5e-08	19	1.1e+03	3.0	no
27	-0.0133	-0.0516	67.9	6.7	0.32	3.1e+03	8.0	7.2e-08	26	1.8e+02	17	no
28	-0.0285	-0.0714	48.8	7.5	0.38	4.5e+03	4.9	1.6e-08	30	8.8e+02	5.1	yes
29	-0.0214	-0.0671	37.3	10	0.32	7.1e+03	4.4	8.2e-09	48	2.5e+03	2.8	yes
30	-0.0151	-0.0488	56.5	7.3	0.20	2.3e+03	8.9	1.1e-08	80	1.6e+03	1.5	no
31	-0.0022	-0.0728	75.6	4.3	0.18	6.7e+02	5.7	1.0e-08	30	6.8e+02	0.99	no
32	-0.0324	-0.0758	48.8	2.4	0.19	2.4e+02	5.2	5.2e-09	26	5.0e+02	0.47	no
33	-0.0036	-0.0705	71.8	7.4	0.20	2.3e+03	5.1	1.6e-08	26	2.4e+02	9.6	no
34	-0.0083	-0.08516	14.4	9.2	0.43	7.6e+03	5.4	7.8e-09	55	3.9e+03	1.9	yes
35	-0.0054	-0.0813	29.7	6.9	0.25	2.5e+03	5.1	6.1e-09	55	2.6e+03	0.96	yes
36	-0.0053	-0.0636	56.5	8.5	0.38	5.9e+03	5.0	8.0e-09	38	1.5e+03	3.9	no
37	-0.0058	-0.0744	75.6	3.1	0.25	5.2e+02	4.2	5.8e-09	28	7.3e+02	0.71	yes

## References

- Amo-Baladrón, M. A., Martín-Pintado, J., & Martín, S. 2011, *A&A*, 526, A54
- An, D., Ramírez, S. V., Sellgren, K., Arendt, R. G., Adwin B. A. C., Robitaille, T. P., Schultheis, M., Cotera, A. S., Smith, H. A. & Stolovy, S. R., 2011, *ApJ*, 736, id133
- Bally, J., Stark, A. A., Wilson, R. W., & Henkel, C., 1987, *ApJS*, 65, 13
- Crutcher, R. M., Roberts, D. A., Mehringer, D. M., & Troland, T. H., 1996b, *ApJ*, 462, L79
- Dumas, G., Vaupré, S., Ceccarelli, C., Hily-Blant, P., Dubus, G., Montmerle, T., & Gabici, S. 2014, *ApJL*, 786, id L24
- Ekers, R. D., van Gorkom, J. H., Schwarz, U. J., & Goss, W. M., 1983, *A&A*, 122, 143
- Figer, D. F.; McLean, I. S., & Morris, M., 1999, *ApJ*, 514, 202
- Figer, D. F. Najarro, F., Gilmore, D., Morris, M. Kim, S. S.; Serabyn, E., McLean, I. S., Gilbert, A. M., Graham, J. R., Larkin, J. E., Levenson, N. A., & Teplitz, H. I. 2002, *ApJ*, 581, 258
- Fukui, Y., Ohama, A., Hanaoka, N., Furukawa, N., Torii, K., Dawson, J. R., Mizuno, N., Hasegawa, K., Fukuda, T., Soga, S., Moribe, N., Kuroda, Y., Hayakawa, T., Kawamura, A., Kuwahara, T., Yamamoto, H., Okuda, T., Onishi, T., Maezawa, H., & Mizuno, A. 2014, *ApJ*, 780, 36
- Furukawa, N., Dawson, J. R., Ohama, A., Kawamura, A., Mizuno, N., Onishi, T., & Fukui, Y. 2009, *ApJ*, 696, L115
- Goss, W. M., Schwarz, U. J., van Gorkom, J. H., & Ekers, R. D., 1985, *MNRAS*, 215, 69
- Habe, A. & Ohta, K. 1992, *PASJ*, 44, 203
- Handa, T., Sakano, M., Naito, S., Hiramatsu, M., & Tsuboi, M. 2006, *ApJ*, 636, 261
- Hasegawa, T., Sato, F., Whiteoak, J.B., Miyawaki, R., 1994, *ApJL*. 429, L77
- Hasegawa, T., Arai, T., Yamaguchi, N., Sato, F., 2008, *Ap&SS*, 313, 91
- Inoue, T., & Fukui, Y. 2013, *ApJ*, 774, L31
- Johnstone, D. & Bally, J. 1999, *ApJ*, 510, L49
- Krumholz, M. R., Klein, R. I., McKee, C. F., Offner, S. S. R., & Cunningham, A. J., 2007, *Science*, 5915, 754.
- Liu, H. B., Ho, P. T. P., Wright, M. C. H., Su, Y.-N., Hsieh, P.-Y., Sun, A.-L., Kim, S.S., & Minh, Y. C., 2013, *ApJ*, 770, id44.
- Martín, S., Martín-Pintado, J., Montero-Castaño, M., Ho, P. T. P., & Blundell, R. 2012 *A&A*, 539, A29
- Mills, E., Morris, M. R., Lang, C. C., Dong, H., Wang, Q. D., Cotera, A., & Stolovy, S. R., 2011, *ApJ*, 735, 84
- Mills, E.A.C. & Morris, M.R., 2013, *ApJ*, 772, 105
- Miyazaki, A., & Tsuboi, M., 2000, *ApJ*, 536 357
- Morris, M. R., 1993, *ApJ*, 408, 496
- Morris, M., & Serabyn, E. 1996, *AAR&A*, 34, 645

Muñoz, D. J., Mardones, D., Garay, G. Rebolledo, D, Brooks, K., & Bontemps, S. 2007, ApJ, 668, 906

Nagahama, T., Mizuno, A., Ogawa, H., & Fukui, Yasuo 1998, AJ, 116, 336

Namekata, D. & Habe, A. 2011, ApJ, 731, 57

Niederhofer, F., Humphreys, E. M. L., & Goddi, C. 2012, A&A, 548, A69

Pierce-Price, D. et al., 2000, ApJL, 545, L121

Pihlström, Y. M., Sjouwerman, L. O., & Fish, V. L. 2011, ApJ, 739, L21

Pineda, J. E., Rosolowsky, E. W., Goodman, A. A., 2009, ApJL, 699,134

Plambeck, R. L., Wright, M. C. H., Friedel, D. N., Widicus Weaver, S. L., Bolatto, A. D., Pound, M. W.,  
Woody, D. P., Lamb, J. W., & Scott, S. L. 2009, ApJL, 704, L25

Sakamoto, K., Mao, R-Q, Matsushita, S., Peck, A. B., Sawada, T., & Wiedner, M. C. 2011, ApJ, 735, 19

Takahira, K., Tasker, E. J., &Habe, A., 2014, ApJ, 793, 63

Tatematsu, K., Umemoto, T., Kameya, O., Hirano, N., Hasegawa, T., Hayashi, M., Iwata, T., Kaifu, N.,  
Mikami, H., Murata, Y., Nakano, M., Nakano, T., Ohashi, N., Sunada, K., Takaba, H., & Yamamoto,  
S. 1993, ApJ, 404, 643

Torii, K., Enokiya, R., Sano, H., Yoshiike, S., Hanaoka, N., Ohama, A., Furukawa, N., Dawson, J. R., Moribe,  
N., Oishi, K., Nakashima, Y., Okuda, T., Yamamoto, H., Kawamura, A., Mizuno, N., Maezawa, H., Onishi,  
T., Mizuno, A., & Fukui, Y. 2011ApJ, 738, 46

Tsuboi, M., Ukita, N., & Handa, T. 1997, ApJ, 481, 263

Tsuboi, M., Handa, T., & Ukita, N., 1999, ApJS, 120, 1

Tsuboi, M., Miyazaki, A., & Okumura, S. K. 2009, PASJ, 61, 29

Tsuboi, M., Tadaki, K-I., Miyazaki, A., & Handa, T. 2011, PASJ, 63, 763

Tsuboi, M., Tadaki, K-I., Miyazaki, A., & Handa, T. 2012, PASJ, 64, id 64

Tsuboi, M. & Miyazaki, A., 2012, PASJ, 64, id 111

Uchida, K.I. & Güsten, R., 1995, A&A, 298, 471

Usero, A., García-Burillo, S., Martín-Pintado, J., Fuente, A., & Neri, R. 2008, New Astronomy Reviews, 51,  
75

van der Tak, F.F.S., Black, J.H., Schöier, F.L., Jansen, D.J., & van Dishoeck, E.F., 2007, A&A, 468, 627

Williams, J. P., de Geus, E. J. & Blitz, L. 1994, ApJ, 428, 693

Yusef-Zadeh, F., Morris, M. 1987a, ApJ, 320, 545

Yusef-Zadeh et al. 2001 ApJ, 560, 749

Yusef-Zadeh, F., Lacy, J. H., Wardle, M., Whitney, B., Bushouse, H., Roberts, D. A., & Arendt, R. G. 2010,  
ApJ, 725, 1429

Yusef-Zadeh, F., Cotton, W., Viti, M., Wardle, M., & Royster, M. 2013, ApJL, 764, L19

Zhao, J-H, Morris, M. R.& Goss, W. M. 2013, ApJ, 777.146

Ziurys, L. M., Friberg, P., & Irvin, W. M. 1989, ApJ, 341, 857